ACS OMEGA

http://pubs.acs.org/journal/acsodf

Article

Hydration of LiOH and LiCl—Near-Infrared Spectroscopic Analysis

Masato Takeuchi,* Ryo Kurosawa, Junichi Ryu, and Masaya Matsuoka

Cite This: *ACS Omega* 2021, 6, 33075−33084

Read Online

ACCESS | Metrics & More | Article Recommendations | Supporting Information

ABSTRACT: The hydration behavior of LiOH, $LiOH{\cdot}H_2O$, and LiCl was observed by near-infrared (NIR) spectroscopy. Anhydrous LiOH showed two absorption bands at 7340 and 7171 cm^{-1}. These NIR bands were assigned to the first overtone of surface hydroxyls and interlayer hydroxyls of LiOH, respectively. $LiOH{\cdot}H_2O$ showed two absorption bands at 7137 and 6970 cm^{-1}. These NIR bands were assigned to the first overtone of interlayer hydroxyls and H_2O molecules coordinated with Li^+, respectively. The interlayer OH^- and the coordinated H_2O of $LiOH{\cdot}H_2O$ were not modified even when the $LiOH{\cdot}H_2O$ was exposed to air. In contrast, anhydrous LiOH was slowly hydrated for several hours, to form $LiOH{\cdot}H_2O$ under ambient conditions (RH 60%). Kinetic analysis showed that the hydration of the interlayer OH^- of LiOH proceeded as a second-order reaction, indicating the formation of intermediate species—$[Li(H_2O)_x(OH)_4]^{3-}$ (x = 1 or 2). However, the hydration of the LiOH surface did not follow a second-order reaction because the chemisorption of H_2O molecules onto the defect sites of the LiOH surface does not need to crossover the energy barrier. Furthermore, we succeeded in observing the hydration of deliquescent LiCl, including the formation of LiCl solution for several minutes by NIR spectroscopy.

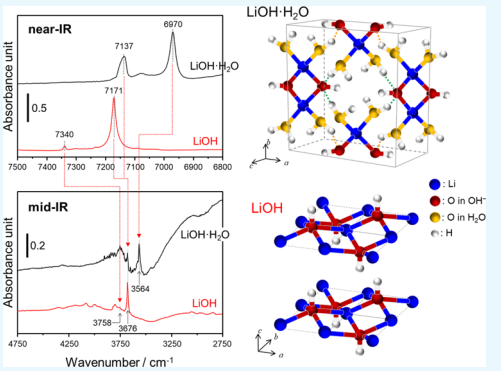

INTRODUCTION

Carbon dioxide and non-carbon greenhouse gas emissions due to human activities cause climate change and temperature rise in a global scale.[1,2] In addition to the effective reduction of CO_2, energy conservation policies have focused on the economic use of renewable energy and unutilized thermal energy sources. Particularly, chemical heat storage or chemical heat pump materials have received attention because of their high energy storage density and long-term storage period.[3−8] For example, $Mg(OH)_2$ decomposes at 350−400 °C to yield MgO and H_2O. Considering the specific heat capacity of $Mg(OH)_2$ (1.78 kJ/kg·K at 600 K) and the decomposition enthalpy (ΔH = 81 kJ/mol) of $Mg(OH)_2$, the total energy to obtain 0.685 kg of MgO and 0.315 kg of H_2O from 1 kg of $Mg(OH)_2$ can be estimated to be approximately 1289 kJ.[3,4,9] In other words, 1 kg of $Mg(OH)_2$ can store the thermal energy obtained by operating an electric heater (1 kW) for 21.5 min, although the dehydration reaction temperature must be higher than 350 °C. To improve the efficiency of the chemical heat storage (CHS) system using the $Mg(OH)_2$/MgO material, Li compounds such as LiOH or LiCl catalyze the dehydration reaction of $Mg(OH)_2$ and the hydration of MgO for the effective storage and output of thermal energy at temperatures in the range of 200−300 °C.[3,4,6] In the previous studies, we discussed the contribution of Li compounds to the dehydration of $Mg(OH)_2$ and the hydration of MgO considering the structural changes in $Mg(OH)_2$ and MgO.[10,11] However, the structural changes of the Li compounds correlating with the dehydration behavior of $Mg(OH)_2$ and the hydration of MgO have not been discussed in any studies till date. Furthermore, Kubota *et al.* reported on $LiOH{\cdot}H_2O$ hybridized with various carbon materials;[12−14] in addition, $LiOH{\cdot}H_2O$ hybridized with polyethylene glycol (PEG), or zeolites,[15] works as a chemical heat storage material operating at temperatures below 100 °C. Additionally, they reported that $LiOH{\cdot}H_2O$ could store a thermal energy of 1440 kJ/kg at approximately 70 °C.[16] However, the NIR spectroscopic observations for the structural changes between LiOH and $LiOH{\cdot}H_2O$ under humid conditions have not been reported in detail till date.

Furthermore, rechargeable batteries have been widely studied as carbon-neutral energy sources. In particular, all-solid-state lithium ion batteries, wherein flammable organic electrolytes are replaced with non-flammable inorganic electrolytes, have received much attention for reducing CO_2 emissions.[17−23] In this system, various sulfide-based solid electrolytes, for example, $Li_2S{-}P_2S_5$ glass ceramics and halichalcogenide Li_6PS_5Cl (argyrodite phase) exhibited ultrahigh Li^+ ion conductivity and a wide electrochemical window.[19−21,24−26] Sulfide-based solid electrolytes show high chemical stability in a low humidity atmosphere, indicating that the materials should be administrated under dry air or

Received: September 28, 2021
Accepted: November 16, 2021
Published: November 24, 2021

inert gas flow conditions. However, sulfide-based materials hydrolyze with water in air to generate H_2S gas.[17] Accordingly, various approaches, such as the partial substitution of sulfide moieties with oxides and the addition of oxides to scavenge H_2S, have been proposed to improve the chemical stability.[27,28] In addition, discerning the hydration behavior of these sulfide-based solid electrolytes under humid conditions, to control the H_2S generation and to avoid a depression of Li^+ ion conductivity, is essential. Moreover, $Li[Ni_xCo_yMn_z]O_2$ or $LiNi_{1-x-y}Co_xAl_yO_2$ cathode materials readily react with CO_2 and H_2O in air to yield Li_2CO_3 and LiOH on their surface.[29−34] Although the LiOH formed on the cathode surface is supposed to be in a monohydrate form, the hydration behavior of Li^+-containing units has not been discussed in detail.

A pioneering study in the field of near-infrared (NIR) spectroscopy is a non-destructive analysis of water content in grains in the 1960s.[35,36] This technique has been widely applied in many fields, such as mineralogy, food chemistry, pharmacology, agriculture, and medical sciences. Recently, Li *et al.* reported the direct evidence of water ice on the lunar polar regions by analyzing the reflectance spectra in the NIR region.[37] Furthermore, NIR observations revealed that an asteroid (3200) Phaethon in near-Earth does not contain any hydrated minerals on the surface.[38] We also employed the NIR spectroscopy to determine the correlation between the wettability of material surfaces and their hydrophilic/hydrophobic properties,[39−44] and the adsorption states of NH_3, NH_4^+,[45,46] and hydrazine.[47] In fact, much attention has been paid for *operando* observations of hydrated surfaces of catalysts, polymers, fabrics, and ceramics. The adsorption states of water molecules are conventionally investigated by Fourier-transform infrared (FT-IR) spectroscopy,[48−52] X-ray photoelectron spectroscopy,[53−56] and scanning tunneling microscopy[57−60] in high vacuum chambers. However, the analyses of hydrated materials, aqueous solutions, and water suspensions are challenging, owing to large absorption coefficient of water molecules in the mid-IR region.[42,43,50−52] In contrast, the overtone and combination bands in the NIR region (0.8−2.5 μm) show 10^3−10^2 times smaller absorption coefficients compared to the fundamental vibrations in the mid-IR region (2.5−25 μm).[36,39−44] This advantage of NIR spectroscopy enables the observation of hydrated materials, aqueous solutions, or chemical reactions involving water molecules.

The objective of this study is to perceive the hydration behaviors of Li compounds, such as LiOH and LiCl by NIR spectroscopy. The crystalline phase transition from LiOH (anhydrous) to LiOH·H_2O (monohydrate) is discussed by X-ray diffraction (XRD) measurements. To discern the structural changes of the interlayer (bulk) hydroxyls and the surface hydroxyls independently during the hydration process of LiOH, we employed the NIR spectroscopy. In addition, the kinetic analysis was performed on the experimental results obtained by XRD and NIR spectroscopic analyses. Finally, we attempted to observe the hydration behavior of deliquescent LiCl by NIR spectroscopy.

RESULTS AND DISCUSSION

Figure 1 shows the XRD patterns for the hydration process of anhydrous LiOH, which was obtained by drying the LiOH·H_2O at 150 °C. The XRD patterns of LiOH·H_2O, LiOH, and Li_2CO_3 are shown in Figure S2 in the Supporting Information for reference. The LiOH samples, which were obtained by

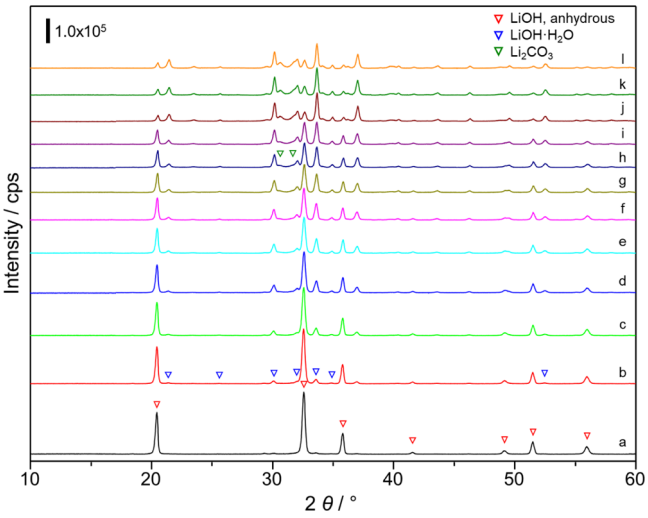

Figure 1. XRD patterns for the hydration process of LiOH (anhydrous). (a) 0 h (dried at 150 °C for 24 h), (b) 0.5, (c) 1, (d) 2, (e) 3, (f) 4, (g) 5, (h) 6, (i) 7, (j) 19, (k) 20, and (l) 23 h.

calcining the LiOH·H_2O at 400 °C for 1 h, or by drying the LiOH·H_2O at 150 °C for 24 h, showed typical diffraction patterns of anhydrous lithium hydroxide.

LiOH before hydration (Figure 1a) showed typical diffraction peaks at 20.5, 32.6, and 35.8°, which are assigned to the (001), (101), and (110) planes of anhydrous LiOH, respectively.[61] In addition, diffraction peaks attributed to Li_2CO_3 were observed for the samples exposed to air surpassing 7 h (Figure 1h−l).[63]

For further discussion, the enlarged XRD patterns in the 2θ ranges of 19.0−23.0° and 29.5−36.5° are shown in Figure 2.

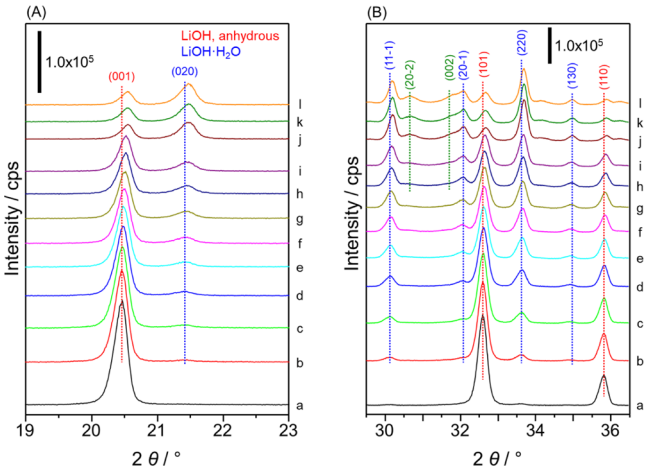

Figure 2. XRD patterns for the hydration process of LiOH (anhydrous) in the 2θ ranges of (A) 19.0−23.0° and (B) 29.5−36.5°. (a) 0 h (dried at 150 °C for 24 h), (b) 0.5, (c) 1, (d) 2, (e) 3, (f) 4, (g) 5, (h) 6, (i) 7, (j) 19, (k) 20, and (l) 23 h.

When anhydrous LiOH was exposed to air at room temperature, the peak intensities of the (001), (101), and (110) planes of LiOH[61] decreased and those of the (020) and (220) planes of LiOH·H_2O[62] increased. Furthermore, the Li_2CO_3 phase[63] was slightly observed at 30.7 and 31.7° for the samples exposed to air for more than 7 h. Interestingly, as the hydration of LiOH proceeded, the diffraction peaks of LiOH

https://doi.org/10.1021/acsomega.1c05379
ACS Omega 2021, 6, 33075−33084

and LiOH·H_2O slightly shifted toward higher angles. This result suggests that the unit cells of LiOH and LiOH·H_2O become smaller owing to the hydrogen bonds of water of crystallization during the hydration process.

The structural model of anhydrous LiOH is shown in Figure 3.

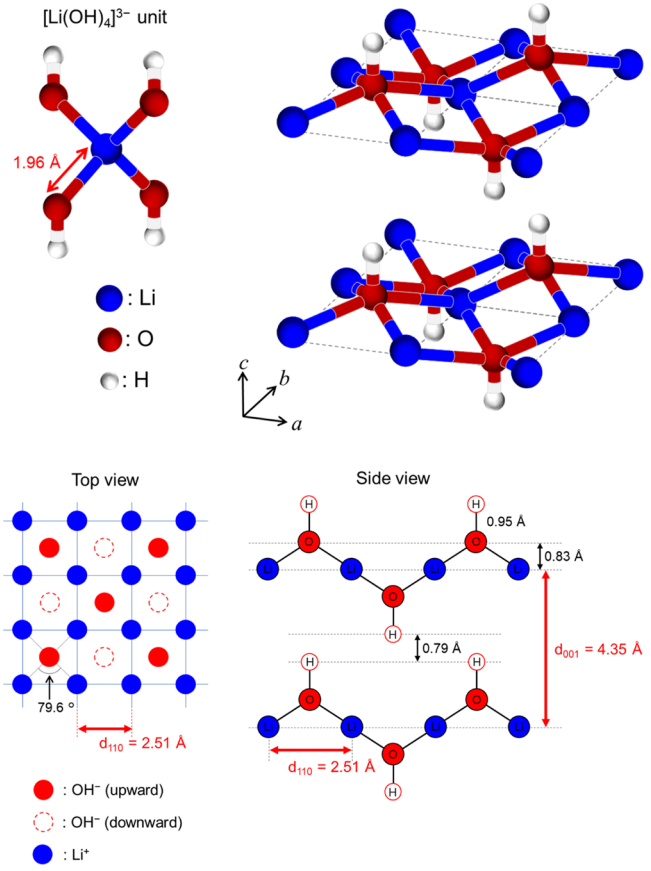

Figure 3. Structural model of LiOH (anhydrous).

Using Bragg's equation, the *d*-spacing values of (001) and (110) planes, observed at 20.5 and 35.8° in the XRD patterns, were calculated to be 4.35, and 2.51 Å, respectively. In a previous study, we discussed the layered structure of $Mg(OH)_2$ by XRD and NIR spectroscopic measurements.[64] LiOH also has a layered structure, wherein several LiOH sheets are stacked.[65,66] Based on these considerations, the d_{001} = 4.35 Å corresponds to the distance between LiOH sheets. Furthermore, the LiOH sheet is formed by connecting several four-sided pyramids of $[Li_4(OH)]^{3+}$ in two dimensions; the upward and downward hydroxyls are alternately arranged as observed in the top view of the LiOH sheet. Because the (110) plane is perpendicular to the (001) plane, the distance between the two red dashed lines in the top view corresponds to the d_{110} spacing of 2.51 Å. Considering the Li−O length of 1.96 Å in tetrahedral LiO_4 units reported by Wenger and Armbruster,[67] the Li−O−Li angle in a triangle on the side of four-sided pyramid (Li_4O unit) was calculated to be 79.6°; consequently, the height of the Li_4O unit was found to be 0.83 Å. As shown in the side view in Figure 3, because the O−H bond length is generally 0.95 Å,[68] the LiOH sheets with upward and downward hydroxyls interact with each other at a distance of 0.79 Å.

The structural model of LiOH·H_2O (a = 7.4153 Å, b = 8.3054 Å, c = 3.1950 Å, β = 110.107°) is shown in Figure 4.

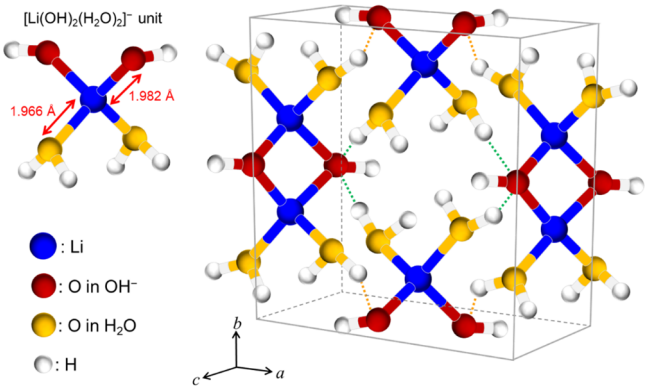

Figure 4. Structural model of LiOH·H_2O (monohydrate).

The LiOH·H_2O contains tetrahedral $[Li(OH)_2(H_2O)_2]^-$ monomer and $[Li_2(OH)_2(H_2O)_4]$ dimer units, wherein Li^+ is coordinated with two OH^- and two H_2O molecules, and two $[Li(OH)_2(H_2O)_2]^-$ units are connected by sharing two OH^-, respectively.[69−72] Gennick and Harmon reported the Li−O lengths in Li^+−OH^- and Li^+−OH_2 were 1.982 and 1.966 Å, respectively.[71] Furthermore, the hydrogen bond distance between the OH^- in $[Li(OH)_2(H_2O)_2]^-$ and the H_2O in $[Li_2(OH)_2(H_2O)_4]$ (four orange dashed lines), and the distance between the H_2O in $[Li(OH)_2(H_2O)_2]^-$ and the OH^- in $[Li_2(OH)_2(H_2O)_4]$ (four green dashed lines) is 2.68 Å.[69] The *d*-spacing of (220) plane, which was observed at 33.4° in Figure 2, was calculated to be 2.68 Å. The interaction between the (220) planes of LiOH·H_2O is predominantly owing to the hydrogen bond networks between the coordinated water of the $[Li(OH)_2(H_2O)_2]^-$ and $[Li_2(OH)_2(H_2O)_4]$ units.

Figure 5 shows the time profiles of the diffraction peak intensities during the hydration process of LiOH.

The intensities of the peaks attributed to the (001), (101), and (110) planes of LiOH appeared to decrease in a similar

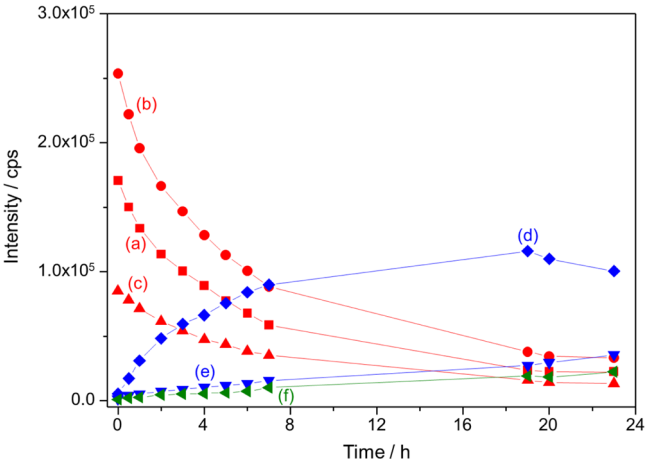

Figure 5. Time profiles for the diffraction intensities during the hydration of LiOH (anhydrous) to LiOH·H_2O. (a) 20.5° [(001) of LiOH], (b) 32.6° [(101) of LiOH], (c) 35.8° [(110) of LiOH], (d) 33.6° [(220) of LiOH·H_2O], (e) 21.5° [(020) of LiOH·H_2O], and (f) 30.6° (Li_2CO_3).

https://doi.org/10.1021/acsomega.1c05379
ACS Omega 2021, 6, 33075−33084

trend. In contrast, the intensity of the peak of (220) plane of $LiOH{\cdot}H_2O$ significantly increased compared to that of the (020) plane. Furthermore, when LiOH was exposed to air, the carbonation of LiOH to form Li_2CO_3 proceeded slowly. To discuss the kinetics of LiOH hydration, the reciprocal plots of the diffraction peak intensities against the hydration time are illustrated in Figure 6.

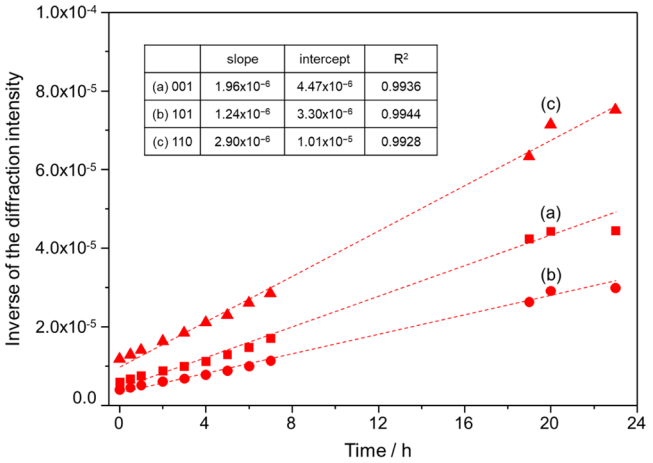

Figure 6. Reciprocal plots of the diffraction intensities during the hydration of LiOH (anhydrous) against the hydration time. (a) 20.5° [(001) of LiOH], (b) 32.6° [(101) of LiOH], and (c) 35.8° [(110) of LiOH].

The linear relationship observed in Figure 6 suggests that the hydration of LiOH to form $LiOH{\cdot}H_2O$ follows a second-order reaction. That is, as the hydration of LiOH proceeds through the formation of intermediate species related to LiOH and H_2O, the reaction rate gradually decreases. Furthermore, the slope values of the straight lines were different, indicating that the hydration rates depend on the crystal planes of LiOH. Particularly, the (110) plane, which is perpendicular to the (001) plane of its layered structure, hydrates 2.3 times faster compared to the (101) plane.

Figure 7 shows the NIR spectra of $LiOH{\cdot}H_2O$ (as-received), LiOH (as-received), and LiOH after drying the $LiOH{\cdot}H_2O$ at 150 °C. $LiOH{\cdot}H_2O$ showed absorption bands at 7137 and 6970 cm^{-1} (Figure 7a) and LiOH showed absorption bands at 7340 and 7171 cm^{-1} (Figure 7c).

As shown in Figure S3, the peak positions of the four NIR absorption bands were identified in the second-derivative spectra. In a previous study on the NIR measurements of $Mg(OH)_2$, three different absorption bands were observed at 7339, 7306, and 7157 cm^{-1} in NIR region. The bands at 7339 and 7306 cm^{-1} were assigned to the first overtone ($2\nu_{OH}$) of surface hydroxyls and that at 7157 cm^{-1} was ascertained to the interlayer hydroxyls of $Mg(OH)_2$. In addition, the NIR absorption band due to water of crystallization in $(MgCO_3)_4{\cdot}Mg(OH)_2{\cdot}5H_2O$ was observed at 6949 cm^{-1}. Based on these considerations, the NIR band at 7340 and 7171 cm^{-1} can be assigned to the surface hydroxyls and interlayer hydroxyls of anhydrous LiOH, respectively. The absorption bands at 7137 and 6970 cm^{-1} can be assigned to the interlayer hydroxyls and coordinated water of $LiOH{\cdot}H_2O$, respectively. As mentioned in a previous study,[64] the wavenumber of $2\nu_{OH}$ is not simply twice of ν_{OH} because of its anharmonicity. Thus, the $\overline{\nu}_{(0\rightarrow1)}$ of fundamental vibration and $\overline{\nu}_{(0\rightarrow2)}$ of 1st overtone are given in eqs 1 and (2)

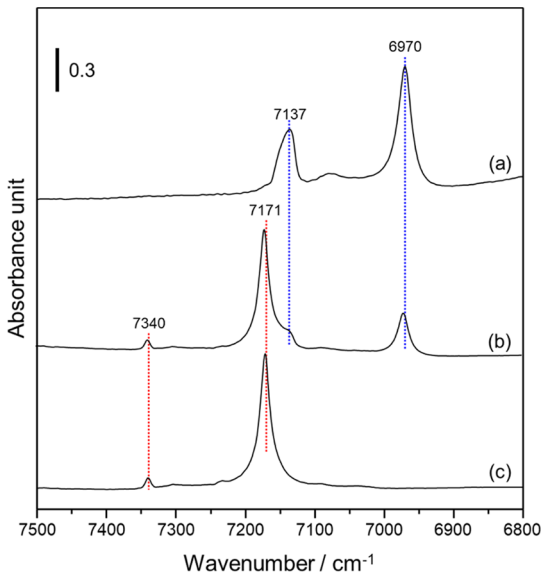

Figure 7. NIR spectra of (a) $LiOH{\cdot}H_2O$ (monohydrate) (as-received), (b) LiOH (anhydrous) (as-received), and (c) LiOH (anhydrous) after drying at 150 °C for 24 h.

$$\overline{\nu}_{(\vec{0}\rightarrow1)} = \overline{\nu}(1 - 2\overline{\chi}) \quad (1)$$

$$\overline{\nu}_{(\vec{0}\rightarrow2)} = 2\overline{\nu}(1 - 3\overline{\chi}) \quad (2)$$

where, $\overline{\nu}$ and $\overline{\chi}$ are the frequency (wavenumber) and anharmonic constant, respectively.

Considering the hydroxyl groups of SiO_2 surface, the $2\nu_{OH}$ and ν_{OH} were observed at 7319 and 3740 cm^{-1}, respectively. From eqs 1 and 2, $\overline{\chi}$ and $\overline{\nu}$ were calculated to be 2.064×10^{-2} and 3990 cm^{-1}, respectively.[64] Using the $\overline{\chi}$ value, the fundamental vibration (ν_{OH}) of LiOH corresponding the NIR bands at 7340 cm^{-1} (surface) and 7171 cm^{-1} (interlayer) was calculated to be 3753 and 3666 cm^{-1}, respectively. In addition, the ν_{OH} of $LiOH{\cdot}H_2O$ corresponding the NIR bands at 7137 and 6970 cm^{-1} was calculated to be 3649 and 3563 cm^{-1}, respectively. Figure S4 shows the FT-IR spectra of $LiOH{\cdot}H_2O$ (as-received) and LiOH, which was obtained by calcining the $LiOH{\cdot}H_2O$ at 400 °C, and by drying the $LiOH{\cdot}H_2O$ at 150 °C. $LiOH{\cdot}H_2O$ showed typical absorption bands at 3676 and 3564 cm^{-1} (Figure S4a), which are assigned to the interlayer OH^- and the coordinated H_2O, respectively.[73−76] In addition, anhydrous LiOH, which were obtained by different pretreatments, showed two absorption bands at 3758 and 3676 cm^{-1} (Figure S4b,c). Correlating the FT-IR spectra of LiOH with the NIR spectra, the absorption bands at 3758 and 3676 cm^{-1} can be assigned to the surface OH^- and the interlayer OH^- of LiOH, respectively.[73−76] However, the FT-IR measurements using a mid-IR light could not distinguish the different interlayer OH^- of LiOH and $LiOH{\cdot}H_2O$. Furthermore, LiOH (as-received) showed four absorption bands owing to LiOH and $LiOH{\cdot}H_2O$ (Figure 7b). This indicates that LiOH in a new reagent bottle (without drying treatment in the laboratory) contains 10−20% of $LiOH{\cdot}H_2O$. Generally, H_2O molecules show broad absorption bands in NIR regions depending on the hydrogen-bond networks, for example, liquid phase water at temperatures near its boiling and freezing points shows absorption bands at 7020 and 6880 cm^{-1}, respectively.[36,39−44] In contrast, the water of crystallization in $LiOH{\cdot}H_2O$ showed a sharp absorption band at 6970 cm^{-1}. As

https://doi.org/10.1021/acsomega.1c05379
ACS Omega 2021, 6, 33075−33084

discussed in the structural model of LiOH·H_2O, the rotation of H_2O molecules, which are directly coordinated to Li^+, is restricted because of the hydrogen bonds.

Figure 8 shows the NIR spectra for the hydration process of LiOH·H_2O. The second-derivative spectra corresponding to the NIR spectra are shown in Figure S5.

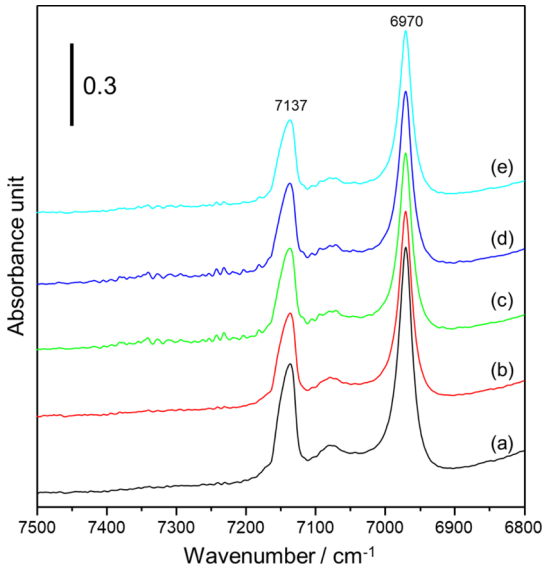

Figure 8. NIR spectra for the hydration process of LiOH·H_2O (monohydrate). (a) 0, (b) 1, (c) 2, (d) 3, and (e) 15 h.

When LiOH·H_2O was exposed to air at room temperature (RH 60%) for 15 h, the changes in the spectral line shapes due to the interlayer hydroxyls (7137 cm^{-1}) and the water of crystallization (6970 cm^{-1}) were insignificant. Evidently, LiOH·H_2O (monohydrate form) was confirmed to not deliquesce even under air conditions.

In contrast, Figure 9 shows the NIR spectra for the hydration process of LiOH, which was obtained by drying the LiOH at 150 °C for 24 h. The second-derivative spectra corresponding to the NIR spectra are shown in Figure S6.

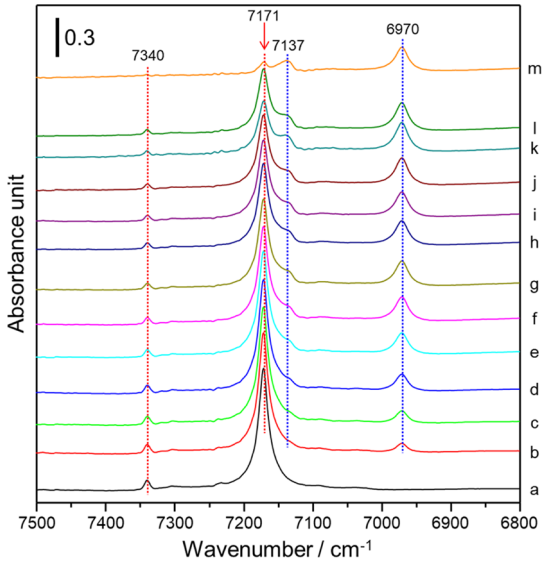

Figure 9. NIR spectra for the hydration process of LiOH (anhydrous). (a) 0 h (dried at 150 °C for 24 h), (b) 15 min, (c) 30 min, (d) 1 h, (e) 2 h, (f) 3 h, (g) 4 h, (h) 5 h, (i) 6 h, (j) 8 h, (k) 10 h, (l) 12 h, and (m) 24 h.

As the spectrum 9a was recorded within 1 min after taking out the well-dried LiOH sample from the drying oven at 150 °C, a similar spectrum as that of anhydrous LiOH (Figure 7c) was observed. However, when the well-dried LiOH sample was placed in air at room temperature (RH 60%) for 30 min, the absorption band due to the water of crystallization in LiOH·H_2O was observed at 6970 cm^{-1}. As the LiOH sample was exposed to air for longer duration, the absorption bands due to LiOH·H_2O at 7137 and 6970 cm^{-1} increased and those owing to LiOH at 7340 and 7171 cm^{-1} gradually decreased. These results clearly indicate that H_2O molecules are intercalated within the layers of LiOH to produce LiOH·H_2O.

As shown in Figure 10, the hydration behavior of anhydrous LiOH was analyzed by the time profile for the peak intensities of the second-derivative spectra.

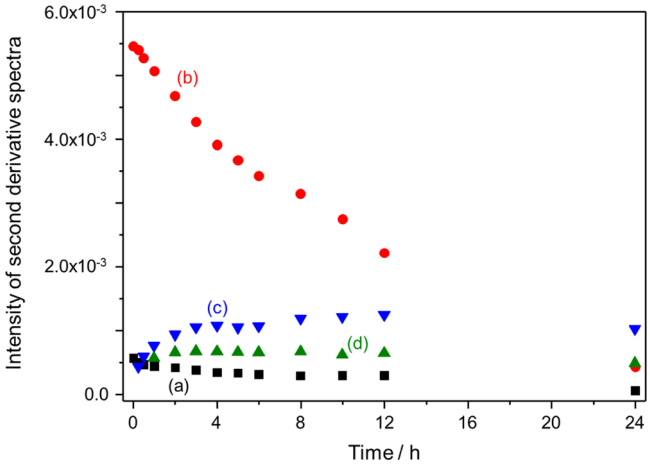

Figure 10. Time profiles for the absorption intensities (second-derivative spectra) during hydration of LiOH (anhydrous). (a) 7340 cm^{-1} (OH^- of LiOH surface), (b) 7171 cm^{-1} (interlayer OH^- of LiOH), (c) 6970 cm^{-1} (coordination H_2O of LiOH·H_2O), and (d) 7137 cm^{-1} (interlayer OH^- of LiOH·H_2O).

The formation of Li_2CO_3 was observed by XRD measurements (Figures 1 and 2); however, the carbonate species were hardly observed by NIR spectroscopy. For further discussion on the kinetics of LiOH hydration, the reciprocal plots of the peak intensities of second-derivative spectra at 7340 and 7171 cm^{-1} against the hydration time are illustrated in Figure 11.

The absorption component at 7171 cm^{-1} showed a linear relationship, indicating that hydration of the interlayer OH^- of LiOH follows a second-order reaction. Therefore, the hydration reaction of interlayer OH^- can be expressed as

$$[Li(OH)_4]^{3-} + 2H_2O \rightarrow [Li(H_2O)_x(OH)_4]^{3-} \rightarrow [Li(H_2O)_2(OH)_2]^- + 2OH^- \quad (3)$$

When the $[Li(OH)_4]^{3-}$ unit of the LiOH surface is converted to the $[Li(OH)_2(H_2O)_2]^-$ of LiOH·H_2O, an intermediate species—$[Li(H_2O)_x(OH)_4]^{3-}$ (x = 1 or 2) can be proposed. Furthermore, this reaction can also be denoted as the substitution reaction of OH^- of the $[Li(OH)_4]^{3-}$ by H_2O molecules.[77] As shown in Figure 6, the hydration rate of the interlayer OH^- of LiOH gradually decreases. This typical

https://doi.org/10.1021/acsomega.1c05379
ACS Omega 2021, 6, 33075−33084

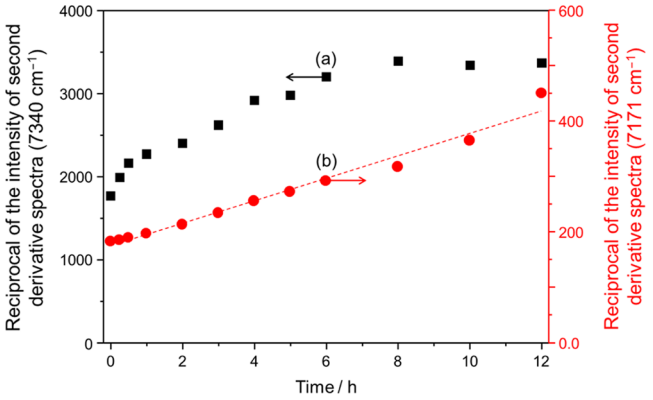

Figure 11. Reciprocal plots of the absorption intensities (second-derivative spectra) of LiOH (anhydrous) against the hydration time. (a) 7340 cm^{-1} (OH^- of LiOH surface), and (b) 7171 cm^{-1} (interlayer OH^- of LiOH).

feature of second-order reaction can be explained by the formation of intermediate species associated with the LiOH and H_2O. These discernments support the assignment of the NIR absorption band at 7171 cm^{-1} to the interlayer OH^- of anhydrous LiOH. In contrast, the hydration of the LiOH surface (7340 cm^{-1}) did not follow a second-order reaction. Considering the pattern of the reciprocal plots, the hydration of the LiOH surface proceeded rapidly in the early stages and eventually stabilized. Thus, the hydration reaction of LiOH surface can be expressed as

$$[Li(OH)_{4-x}(V_{OH}^{\cdot})_x]^{(3-x)-} + xH_2O \rightarrow [Li(OH)_{4-x}(H_2O)_x]^{(3-x)-} \quad (x = 1,2,3,4) \qquad (4)$$

In this reaction, the $V_{OH}^{\bullet}$ represents defect sites of OH^- located on the LiOH surface. The reaction, in the case of $x = 4$, which corresponds to a hydration of free Li^+,[78] does not occur on the LiOH surface. In the case of $x = 3$, the charge of $[Li(OH)(H_2O)_3]$ unit becomes neutral, suggesting the instability of $LiOH{\cdot}H_2O$ lattice as an ionic crystal. Thus, the reactions, in the case of $x = 1$ or 2 are plausible as hydration processes of LiOH surface. Furthermore, these reactions can be rendered as the chemisorption of H_2O molecules onto the defect sites of LiOH surface, without the formation of intermediate species. Consequently, the hydration of LiOH surface does not follow a second-order reaction.

Finally, the NIR spectra for the hydration process of LiCl, which were obtained by drying the LiCl at 150 °C for 24 h, are shown in Figure 12. The spectrum 12(a) was recorded within 1 min after taking out the well-dried LiCl sample from the drying oven at 150 °C. However, less-intense absorption bands are observed at 6787 and 5027 cm^{-1}.

These NIR bands are assigned to a first overtone ($2\nu_{OH}$) and ($\nu_{OH} + \delta$) combination band of H_2O molecules directly coordinated with Li^+ of LiCl, respectively. When the LiCl sample was exposed to air, the intensities of the broad absorption bands in the range of 7200−6000 cm^{-1} and at 5162 cm^{-1} significantly increased, in addition to the NIR bands owing to the coordinated H_2O. These absorption bands are assigned to a first overtone ($2\nu_{OH}$) and ($\nu_{OH} + \delta$) combination of H_2O in the liquid-phase. It is challenging to observe the hydration behavior of these deliquescent materials by FT-IR spectroscopy because of the large absorption coefficient of H_2O molecule. However, the overtone and combination bands

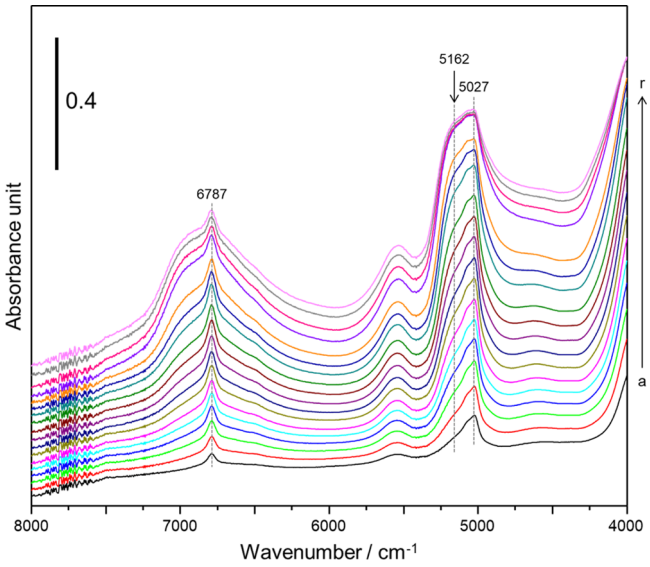

Figure 12. NIR spectra for the hydration process of LiCl (anhydrous). (a) 0 min (dried at 150 °C for 24 h), (b) 1, (c) 2, (d) 3, (e) 4, (f) 5, (g) 6, (h) 7, (i) 8, (j) 9, (k) 10, (l) 12, (m) 14, (n) 16, (o) 18, (p) 20, (q) 22, and (r) 24 min.

in NIR regions show smaller absorption coefficients compared to the fundamental vibrations.[36,39−44] The advantage of NIR spectroscopy facilitated us to observe the hydration behavior of deliquescent LiCl. The second-derivative spectra corresponding to the NIR spectra are shown in Figure S7. As the effects of broad absorption bands owing to H_2O in the liquid phase are excluded in the second-derivative analyses, only the effects of the coordinated H_2O onto Li^+ are discussed. Therefore, the time profiles for the peak intensities of second-derivative spectra at 6787 and 5015 cm^{-1} are illustrated in Figure 13. In addition, the amount of H_2O in the liquid phase was estimated from the absorption peak area in the range of 7200−6000 cm^{-1}.

Interestingly, the amount of the coordinated H_2O to Li^+ increased until 8−12 min but subsequently decreased (Figure 13a,b). Furthermore, the amount of H_2O in the liquid phase monotonically increased until 18 min and then leveled off

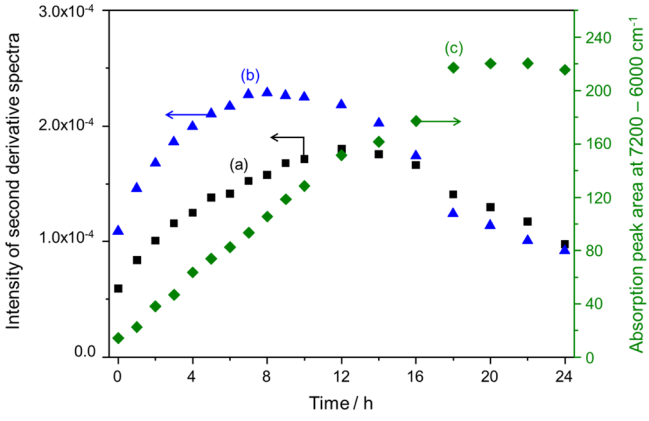

Figure 13. Time profiles for the absorption peak intensities (second-derivative spectra) at (a) 6787 cm^{-1} (coordination H_2O of $LiCl{\cdot}H_2O$), (b) 5015 cm^{-1} (coordination H_2O of $LiCl{\cdot}H_2O$), and (c) absorption peak area at 7200−6000 cm^{-1} owing to the amount of H_2O in the liquid phase.

https://doi.org/10.1021/acsomega.1c05379
ACS Omega 2021, 6, 33075−33084

(Figure 13c). These results indicate that the coordinated H_2O onto Li^+ decreases after the formation of LiCl aqueous solution. In fact, small amounts of droplets of the LiCl aqueous solution was confirmed on the sample holder of FT-NIR spectrophotometer.

CONCLUSIONS

The hydration behaviors of LiOH, LiOH·H_2O, and LiCl were investigated using NIR spectroscopy. The anhydrous LiOH showed two absorption bands at 7340 and 7171 cm^{-1}, which correspond to the surface OH^- and the interlayer OH^- of LiOH, respectively. The LiOH·H_2O exhibited two absorption bands at 7137 and 6970 cm^{-1}, which correspond to the interlayer OH^- and the H_2O of crystallization of LiOH·H_2O, respectively. The fundamental vibration (ν_{OH}) of LiOH and LiOH·H_2O corresponding to the NIR bands at 7340, 7171, 7137, and 6970 cm^{-1} was estimated to be 3753, 3666, 3649, and 3563 cm^{-1}, respectively. However, both the interlayer hydroxyls of LiOH and LiOH·H_2O were observed at 3676 cm^{-1}, indicating the incapability to distinguish their differences by FT-IR measurements.

When the LiOH·H_2O was exposed to air at room temperature (RH 60%), the modification in the interlayer OH^- and the coordinated H_2O was insignificant. However, when anhydrous LiOH was exposed to air for several hours at room temperature (RH 60%), the LiOH was slowly hydrated to form LiOH·H_2O. Kinetic analysis showed that the hydration of the interlayer OH^- of LiOH proceeded as a second-order reaction; however, that of the LiOH surface did not. Finally, we succeeded in observing the hydration behavior of deliquescent LiCl using NIR spectroscopy. When the well-dried LiCl was exposed to air, the coordinated H_2O, which was observed at 6787 cm^{-1}, and H_2O in the liquid phase significantly increased in several minutes. The wavenumbers and assignments of the NIR absorption bands, which were observed for LiOH, LiOH·H_2O, and LiCl, are summarized in Table 1.

Table 1. Wavenumbers and Assignments of the NIR Absorption Bands of LiOH (anhydrous), LiOH·H_2O (monohydrate), and LiCl·H_2O (monohydrate)

wavenumber/ cm^{-1}	assignments	
7340	OH^- in $[Li(OH)_4]^{3-}$	LiOH (surface)
7171	OH^- in $[Li(OH)_4]^{3-}$	LiOH (interlayer)
7137	OH^- in $[Li(OH)_2(H_2O)_2]^-$ and/or $[Li_2(OH)_2(H_2O)_4]$	LiOH·H_2O (interlayer)
6970	H_2O of crystallization in $[Li(OH)_2(H_2O)_2]^-$ and/or $[Li_2(OH)_2(H_2O)_4]$	LiOH·H_2O (bulk)
6787	H_2O of crystallization in LiCl·H_2O	LiCl·H_2O (bulk)

Analyzing more complicated hydration and dehydration behaviors of $Mg(OH)_2$ modified with various Li compounds is the future prospect of this study.

EXPERIMENTAL SECTION

Chemicals Used. Lithium hydroxide monohydrate (LiOH·H_2O) and lithium chloride anhydrous (LiCl) in reagent grade were purchased from Nacalai Tesque, Inc. (Japan). The reagent grade lithium hydroxide anhydrous (LiOH) was purchased from Tokyo Chemical Industry Co., Ltd. (Japan). As discussed in the following sections, the anhydrous LiOH in a new reagent bottle contained 10−20% of LiOH·H_2O (monohydrate). Consequently, completely dehydrated LiOH was obtained by calcining the LiOH·H_2O at 400 °C for 1 h, or drying the LiOH·H_2O at 150 °C for 24 h. Anhydrous LiOH, anhydrous LiCl, and LiOH monohydrate are referred as LiOH, LiCl, and LiOH·H_2O, respectively.

Characterization. *XRD and Thermogravimetry-Differential Thermal Analysis.* The crystal structures of the samples were analyzed using an X-ray diffractometer (Ultima IV, Rigaku, Japan) with Cu Kα radiation (1.5406 Å). The hydration process of the anhydrous LiOH, which was obtained by drying the LiOH·H_2O at 150 °C for 24 h, under ambient conditions was analyzed the XRD measurements. The XRD patterns were obtained at a scan rate of 10°/min to avoid the formation of hydrate species during the measurements. Thermogravimetry-differential thermal analysis (TG-DTA) measurement was performed for LiOH·H_2O using a thermobalance (TGD−9600 series, Advance Riko, Inc., Japan) at a heating rate of 10 °C/min up to 600 °C with a continuous flow of Ar gas (100 mL/min).

NIR Measurements of the Hydration of Anhydrous LiOH and LiCl. Prior to the NIR spectroscopic measurements, anhydrous LiOH and LiCl in the new reagent bottles were pretreated in a drying oven at 150 °C for 24 h. Figure S1 in the Supporting Information shows the TG-DTA profile of LiOH·H_2O. As the molecular weight of LiOH·H_2O is 41.95, the weight loss of 43% corresponds to the removal of crystallization H_2O to form anhydrous LiOH. Consequently, the pretreatment temperature for obtaining anhydrous LiOH was determined to be 150 °C. Therefore, the anhydrous LiOH sample (20 mg) was placed on a diffuse reflectance measurement unit (CaF_2 window) and the NIR spectrum was immediately recorded at room temperature using a Fourier transform-near infrared (FT-NIR) spectrophotometer (FT/IR-4700, JASCO, Japan, WI lamp, InGaAs detector, baseline calibration: Al plate). The duration to take out the dehydrated sample from the drying oven and start the NIR measurement was approximately 1 min. Then, the sample was stored in air at 25 °C and relative humidity (RH) of 60%. The NIR spectra of the samples were recorded at periodic hydration time intervals. For comparison, the hydration behavior of LiOH·H_2O was observed in the same procedure.

FT-IR Measurements (Mid-IR Region) of LiOH·H_2O and LiOH. To verify the assignments of NIR absorptions, FT-IR spectra (mid-IR region) of LiOH·H_2O and LiOH were recorded using a FT-IR spectrophotometer (FT/IR-4200, JASCO, Japan, baseline calibration: CaF_2). Prior to the measurements, the LiOH·H_2O (as-received), or LiOH (calcined the LiOH·H_2O at 400 °C for 1 h, or dried the LiOH·H_2O at 150 °C for 24 h) was mixed with a CaF_2 powder (sample/CaF_2 = 1:5). These samples were placed on a diffuse reflectance unit (CaF_2 window) and the FT-IR spectra were quickly recorded at room temperature.

ASSOCIATED CONTENT

Supporting Information

The Supporting Information is available free of charge at https://pubs.acs.org/doi/10.1021/acsomega.1c05379.

https://doi.org/10.1021/acsomega.1c05379
ACS Omega 2021, 6, 33075−33084

TG-DTA profile of $LiOH·H_2O$; XRD patterns of $LiOH·H_2O$, LiOH, and Li_2CO_3; second-derivative spectra corresponding to the NIR spectra of $LiOH·H_2O$, and LiOH; FT-IR spectra (mid-IR region) of $LiOH·H_2O$, and LiOH; and second-derivative spectra corresponding to the NIR spectra (hydration process of $LiOH·H_2O$, LiOH, and LiCl) (PDF)

AUTHOR INFORMATION

Corresponding Author

Masato Takeuchi − *Department of Applied Chemistry, Graduate School of Engineering, Osaka Prefecture University, Osaka 599-8531, Japan;* orcid.org/0000-0003-3851-9409; Email: masato-t@chem.osakafu-u.ac.jp

Authors

Ryo Kurosawa − *Graduate School of Engineering, Chiba University, Chiba 263-8522, Japan*

Junichi Ryu − *Graduate School of Engineering, Chiba University, Chiba 263-8522, Japan;* orcid.org/0000-0003-2248-8644

Masaya Matsuoka − *Department of Applied Chemistry, Graduate School of Engineering, Osaka Prefecture University, Osaka 599-8531, Japan*

Complete contact information is available at: https://pubs.acs.org/10.1021/acsomega.1c05379

Notes

The authors declare no competing financial interest.

ACKNOWLEDGMENTS

The authors would like to thank Editage (www.editage.com) for English language editing.

REFERENCES

(1) Fyfe, J. C.; Meehl, G. A.; England, M. H.; Mann, M. E.; Santer, B. D.; Flato, G. M.; Hawkins, E.; Gillett, N. P.; Xie, S.-P.; Kosaka, Y.; Swart, N. C. Making sense of the early-2000s warming slowdown. *Nat. Clim. Change* **2016**, *6*, 224−228.

(2) Cook, J.; Oreskes, N.; Doran, P. T.; Anderegg, W. R. L.; Verheggen, B.; Maibach, E. W.; Carlton, J. S.; Lewandowsky, S.; Skuce, A. G.; Green, S. A.; Nuccitelli, D.; Jacobs, P.; Richardson, M.; Winkler, B.; Painting, R.; Rice, K. Consensus on consensus: a synthesis of consensus estimates on human-caused global warming. *Environ. Res. Lett.* **2016**, *11*, 048002.

(3) Ishitobi, H.; Hirao, N.; Ryu, J.; Kato, Y. Evaluation of Heat Output Densities of Lithium Chloride-Modified Magnesium Hydroxide for Thermochemical Energy Storage. *Ind. Eng. Chem. Res.* **2013**, *52*, 5321−5325.

(4) Ishitobi, H.; Uruma, K.; Takeuchi, M.; Ryu, J.; Kato, Y. Dehydration and hydration behavior of metal-salt-modified materials for chemical heat pumps. *Appl. Therm. Eng.* **2013**, *50*, 1639−1644.

(5) Nomura, T.; Zhu, C.; Sheng, N.; Saito, G.; Akiyama, T. Microencapsulation of metal-based phase change material for high-temperature thermal energy storage. *Sci. Rep.* **2015**, *5*, 9117.

(6) Kurosawa, R.; Takeuchi, M.; Ryu, J. Comparison of the Effect of Coaddition of Li Compounds and Addition of a Single Li Compound on Reactivity and Structure of Magnesium Hydroxide. *ACS Omega* **2019**, *4*, 17752−17761.

(7) Shkatulov, A.; Krieger, T.; Zaikovskii, V.; Chesalov, Y.; Aristov, Y. Doping magnesium hydroxide with sodium nitrate: A new approach to tune the dehydration reactivity of heat-storage materials. *ACS Appl. Mater. Interfaces* **2014**, *6*, 19966−19977.

(8) McGillicuddy, R. D.; Thapa, S.; Wenny, M. B.; Gonzalez, M. I.; Mason, J. A. Metal-Organic Phase-Change Materials for Thermal Energy Storage. *J. Am. Chem. Soc.* **2020**, *142*, 19170−19180.

(9) Kastiukas, G.; Zhou, X.; Neyazi, B.; Wan, K. T. Sustainable calcination of magnesium hydroxide for magnesium oxychloride cement production. *J. Mater. Civ. Eng.* **2019**, *31*, 04019110.

(10) Kurosawa, R.; Takeuchi, M.; Ryu, J. Fourier-transform infrared analysis of the dehydration mechanism of $Mg(OH)_2$ and chemically modified $Mg(OH)_2$. *J. Phys. Chem. C* **2021**, *125*, 5559−5571.

(11) Kurosawa, R.; Takeuchi, M.; Ryu, J. Fourier-transform infrared and X-ray diffraction analyses of the hydration reaction of pure magnesium oxide and chemically modified magnesium oxide. *RSC Adv.* **2021**, *11*, 24292−24311.

(12) Yang, X.; Huang, H.; Wang, Z.; Kubota, M.; He, Z.; Kobayashi, N. Facile synthesis of graphene oxide-modified lithium hydroxide for low-temperature chemical heat storage. *Chem. Phys. Lett.* **2016**, *644*, 31−34.

(13) Yang, X.; Li, S.; Huang, H.; Li, J.; Kobayashi, N.; Kubota, M. Effect of carbon nanoadditives on lithium hydroxide monohydrate-based composite materials for low temperature chemical heat storage. *Energies* **2017**, *10*, 644.

(14) Kubota, M.; Matsumoto, S.; Matsuda, H. Enhancement of hydration rate of LiOH by combining with mesoporous carbon for low-temperature chemical heat storage. *Appl. Therm. Eng.* **2019**, *150*, 858−863.

(15) Li, S.; Huang, H.; Yang, X.; Bai, Y.; Li, J.; Kobayashi, N.; Kubota, M. Hydrophilic substance assisted low temperature $LiOH·H_2O$ based composite thermochemical materials for thermal energy storage. *Appl. Therm. Eng.* **2018**, *128*, 706−711.

(16) Kubota, M.; Matsumoto, S.; Matsuda, H.; Huang, H. Y.; He, Z. H.; Yang, X. X. Chemical heat storage with $LiOH/LiOH·H_2O$ reaction for low-temperature heat below 373 K. *Adv. Mater. Res.* **2014**, *953*−*954*, 757−760.

(17) Tatsumisago, M.; Nagao, M.; Hayashi, A. Recent development of sulfide solid electrolytes and interfacial modification for all-solid-state rechargeable lithium batteries. *J. Asian Ceram. Soc.* **2013**, *1*, 17−25.

(18) Sang, L.; Bassett, K. L.; Castro, F. C.; Young, M. J.; Chen, L.; Haasch, R. T.; Elam, J. W.; Dravid, V. P.; Nuzzo, R. G.; Gewirth, A. A. Understanding the effect of interlayers at the thiophosphate solid electrolyte/lithium interface for all-solid-state Li batteries. *Chem. Mater.* **2018**, *30*, 8747−8756.

(19) Tsukasaki, H.; Mori, Y.; Otoyama, M.; Yubuchi, S.; Asano, T.; Tanaka, Y.; Ohno, T.; Mori, S.; Hayashi, A.; Tatsumisago, M. Crystallization behavior of the $Li_2S−P_2S_5$ glass electrolyte in the $LiNi_{1/3}Mn_{1/3}Co_{1/3}O_2$ positive electrode layer. *Sci. Rep.* **2018**, *8*, 6214.

(20) Hartley, G. O.; Jin, L.; Bergner, B. J.; Jolly, D. S.; Rees, G. J.; Zekoll, S.; Ning, Z.; Pateman, A. T. R.; Holc, C.; Adamson, P.; Bruce, P. G. Is nitrogen present in $Li_3N·P_2S_5$ solid llectrolytes produced by ball milling? *Chem. Mater.* **2019**, *31*, 9993−10001.

(21) Takahashi, M.; Watanabe, T.; Yamamoto, K.; Ohara, K.; Sakuda, A.; Kimura, T.; Yang, S.; Nakanishi, K.; Uchiyama, T.; Kimura, M.; Hayashi, A.; Tatsumisago, M.; Uchimoto, Y. Investigation of the suppression of dendritic lithium growth with a lithium-iodide-containing solid electrolyte. *Chem. Mater.* **2021**, *33*, 4907−4914.

(22) He, X.; Sun, H.; Ding, X.; Zhao, K. Grain boundaries and their impact on Li kinetics in layered-oxide cathodes for Li-ion batteries. *J. Phys. Chem. C* **2021**, *125*, 10284−10294.

(23) Katzenmeier, L.; Carstensen, L.; Schaper, S. J.; Müller-Buschbaum, P.; Bandarenka, A. S. Characterization and Quantification of Depletion and Accumulation Layers in Solid-State Li + -Conducting Electrolytes Using In Situ Spectroscopic Ellipsometry. *Adv. Mater.* **2021**, *33*, 2100585.

(24) Wang, Z.; Shao, G. Theoretical design of solid electrolytes with superb ionic conductivity: alloying effect on Li^+ transportation in cubic Li_6PA_5X chalcogenides. *J. Mater. Chem. A* **2017**, *5*, 21846−21857.

(25) Xu, H.; Yu, Y.; Wang, Z.; Shao, G. A theoretical approach to address interfacial problems in all-solid-state lithium ion batteries: tuning materials chemistry for electrolyte and buffer coatings based on Li_6PA_5Cl hali-chalcogenides. *J. Mater. Chem. A* **2019**, *7*, 5239−5247.
(26) Delnick, F. M.; Yang, G.; Self, E. C.; Meyer, H. M., III; Nanda, J. Investigation of complex intermediates in solvent-mediated synthesis of thiophosphate solid-state electrolytes. *J. Phys. Chem. C* **2020**, *124*, 27396−27402.
(27) Ohtomo, T.; Hayashi, A.; Tatsumisago, M.; Kawamoto, K. Characteristics of the Li_2O−Li_2S−P_2S_5 glasses synthesized by the two-step mechanical milling. *J. Non-Cryst. Solids* **2013**, *364*, 57−61.
(28) Hayashi, A.; Muramatsu, H.; Ohtomo, T.; Hama, S.; Tatsumisago, M. Improvement of chemical stability of Li_3PS_4 glass electrolytes by adding M_xO_y (M = Fe, Zn, and Bi) nanoparticles. *J. Mater. Chem. A* **2013**, *1*, 6320−6326.
(29) Matsumoto, K.; Kuzuo, R.; Takeya, K.; Yamanaka, A. Effects of CO_2 in air on Li deintercalation from $LiNi_{1-x-y}Co_xAl_yO_2$. *J. Power Sources* **1999**, *81*−*82*, 558−561.
(30) Noh, H.-J.; Youn, S.; Yoon, C. S.; Sun, Y.-K. Comparison of the structural and electrochemical properties of layered $Li[Ni_xCo_yMn_z]O_2$ (x = 1/3, 0.5, 0.6, 0.7, 0.8 and 0.85) cathode material for lithium-ion batteries. *J. Power Sources* **2013**, *233*, 121−130.
(31) Mijung, N.; Lee, Y.; Cho, J. Water adsorption and storage characteristics of optimized $LiCoO_2$ and $LiNi_{1/3}Co_{1/3}Mn_{1/3}O_2$ composite cathode material for Li-ion cells. *J. Electrochem. Soc.* **2006**, *153*, A935−A940.
(32) Faenza, N. V.; Bruce, L.; Lebens-Higgins, Z. W.; Plitz, I.; Pereira, N.; Piper, L. F. J.; Amatucci, G. G. Growth of ambient induced surface impurity species on layered positive electrode materials and impact on electrochemical performance. *J. Electrochem. Soc.* **2017**, *164*, A3727−A3741.
(33) Zou, Y.; Yang, X.; Lv, C.; Liu, T.; Xia, Y.; Shang, L.; Waterhouse, G. I. N.; Yang, D.; Zhang, T. Multishelled Ni-rich $Li(Ni_xCo_yMn_z)O_2$ hollow fibers with low cation mixing as high-performance cathode materials for Li-ion batteries. *Adv. Sci.* **2017**, *4*, 1600262.
(34) Seong, W. M.; Kim, Y.; Manthiram, A. Impact of residual lithium on the adoption of high-nickel layered oxide cathodes for lithium-ion batteries. *Chem. Mater.* **2020**, *32*, 9479−9489.
(35) Williams, P.; Norris, K. *Near-Infrared Technology in the Agricultural and Food Industries*, 2nd Ed.; American Association of Cereal Chemists: St. Paul, Minnesota, USA, 2001.
(36) Chalmers, J. M.; Griffiths, P. R. *Handbook of Vibrational Spectroscopy*; Wiley, 2002; Vol. 3; pp 1817−1837.
(37) Li, S.; Lucey, P. G.; Milliken, R. E.; Hayne, P. O.; Fisher, E.; Williams, J.-P.; Hurley, D. M.; Elphic, R. C. Direct evidence of surface exposed water ice in the lunar polar regions. *Proc. Natl. Acad. Sci. U.S.A.* **2018**, *115*, 8907−8912.
(38) Takir, D.; Kareta, T.; Emery, J. P.; Hanuš, J.; Reddy, V.; Howell, E. S.; Rivkin, A. S.; Arai, T. Near-infrared observations of active asteroid (3200) Phaethon reveal no evidence for hydration. *Nature Commun.* **2020**, *11*, 2050.
(39) Takeuchi, M.; Martra, G.; Coluccia, S.; Anpo, M. Investigations of the structure of H_2O clusters adsorbed on TiO_2 Surfaces by Near-Infrared Absorption Spectroscopy. *J. Phys. Chem. B* **2005**, *109*, 7387−7391.
(40) Takeuchi, M.; Sakamoto, K.; Martra, G.; Coluccia, S.; Anpo, M. Mechanism of photoinduced superhydrophilicity on the TiO_2 photocatalyst surface. *J. Phys. Chem. B* **2005**, *109*, 15422−15428.
(41) Takeuchi, M.; Martra, G.; Coluccia, S.; Anpo, M. Verification of the photoadsorption of H_2O molecules on TiO_2 semiconductor surfaces by vibrational absorption spectroscopy. *J. Phys. Chem. C* **2007**, *111*, 9811−9817.
(42) Takeuchi, M.; Martra, G.; Coluccia, S.; Anpo, M. Evaluation of the Adsorption States of H_2O on Oxide Surfaces by Vibrational Absorption: Near- and Mid-Infrared Spectroscopy. *J. Near Infrared Spectrosc.* **2009**, *17*, 373−384.
(43) Takeuchi, M. Surface analysis of various oxide materials by using NIR spectroscopy −Is silica surface really hydrophilic? *J. Imaging Soc. Jpn.* **2019**, *58*, 633−643.
(44) Kawaguchi, K.; Takeuchi, M.; Yamagawa, H.; Murakami, K.; Nakai, S.; Hori, H.; Ohashi, A.; Hiki, Y.; Suzuki, N.; Sugiyama, S.; Yuzawa, Y.; Kitaguchi, N. A potential therapeutic system for Alzheimer's disease using adsorbents with alkyl ligands for removal of blood amyloid β. *J. Artif. Organs* **2013**, *16*, 211−217.
(45) Takeuchi, M.; Tsukamoto, T.; Kondo, A.; Matsuoka, M. Investigation of NH_3 and NH_4^+ adsorbed on ZSM-5 zeolites by near and middle infrared spectroscopy. *Catal. Sci. Technol.* **2015**, *5*, 4587−4593.
(46) Takeuchi, M.; Tsukamoto, T.; Kondo, A.; Bao, Y.; Matsuoka, M. Near infrared study on the adsorption states of NH_3 and NH_4^+ on hydrated ZSM-5 zeolites. *J. Near Infrared Spectrosc.* **2019**, *27*, 241−249.
(47) Takano, A.; Iseki, Y.; Yanagi, M.; Bao, Y.; Asazawa, K.; Kato, T.; Takeuchi, M. Simultaneous analyses of hydrazine molecules and hydrazinium ions in aqueous solution and adsorbed on catalyst surfaces by near-infrared spectroscopy. *Chem. Lett.* **2019**, *48*, 738−741.
(48) Coluccia, S.; Baricco, M.; Marchese, L.; Martra, G.; Zecchina, A. Surface morphology and reactivity towards CO of MgO particles: FTIR and HRTEM studies. *Spectrochim. Acta* **1993**, *49*, 1289−1298.
(49) Martra, G.; Cacciatori, T.; Marchese, L.; Hargreaves, J. S. J.; Mellor, I. M.; Joyner, R. W.; Coluccia, S. Surface morphology and reactivity of microcrystalline MgO Single and multiple acid−base pairs in low coordination revealed by FTIR spectroscopy of adsorbed CO, CD_3CN and D_2. *Catal. Today* **2001**, *70*, 121−130.
(50) Ryczkowski, J. IR spectroscopy in catalysis. *Catal. Today* **2001**, *68*, 263−381.
(51) Takeuchi, M.; Bertinetti, L.; Martra, G.; Coluccia, S.; Anpo, M. States of H_2O adsorbed on oxides: An investigation by near and mid infrared spectroscopy. *Appl. Catal., A* **2006**, *307*, 13−20.
(52) Takeuchi, M.; Deguchi, J.; Sakai, S.; Anpo, M. Effect of H_2O vapor addition on the photocatalytic oxidation of ethanol, acetaldehyde and acetic acid in the gas phase on TiO_2 semiconductor powders. *Appl. Catal., B* **2010**, *96*, 218−223.
(53) Aita, H.; Hori, N.; Takeuchi, M.; Suzuki, T.; Yamada, M.; Anpo, M.; Ogawa, T. The effect of ultraviolet functionalization of titanium on integration with bone. *Biomaterials* **2009**, *30*, 1015−1025.
(54) Att, W.; Takeuchi, M.; Suzuki, T.; Kubo, K.; Anpo, M.; Ogawa, T. Enhanced osteoblast function on ultraviolet light-treated zirconia. *Biomaterials* **2009**, *30*, 1273−1280.
(55) Knipe, S. W.; Mycroft, J. R.; Pratt, A. R.; Nesbitt, H. W.; Bancroff, G. M. X-ray photoelectron spectroscopic study of water adsorption on iron sulphide minerals. *Geochim. Cosmochim. Acta* **1995**, *59*, 1079−1090.
(56) Zhang, X.; Ptasinska, S. Dissociative adsorption of water on an H_2O/GaAs(100) interface: In situ near-ambient pressure XPS studies. *J. Phys. Chem. C* **2014**, *118*, 4259−4266.
(57) Freund, J.; Halbritter, J.; Hörber, J. K. H. How dry are dried samples? Water adsorption measured by STM. *Microsc. Res. Tech.* **1999**, *44*, 327−338.
(58) Brookes, I. M.; Muryn, C. A.; Thornton, G. Imaging water dissociation on TiO_2(110). *Phys. Rev. Lett.* **2001**, *87*, 266103.
(59) Mezhenny, S.; Maksymovych, P.; Thompson, T. L.; Diwald, O.; Stahl, D.; Walck, S. D.; Yates, J. T., Jr. STM studies of defect production on the TiO_2(110)-(1×1) and TiO_2(110)-(1×2) surfaces induced by UV irradiation. *Chem. Phys. Lett.* **2003**, *369*, 152−158.
(60) Becerra-Toledo, A. E.; Castell, M. R.; Marks, L. D. Water adsorption on $SrTiO_3$(001): I. Experimental and simulated STM. *Surf. Sci.* **2012**, *606*, 762−765.
(61) Li, Z.; Ganapathy, S.; Xu, Y.; Heringa, J. R.; Zhu, Q.; Chen, W.; Wagemaker, M. Understanding the electrochemical formation and decomposition of Li_2O_2 and LiOH with operando X-ray diffraction. *Chem. Mater.* **2017**, *29*, 1577−1586.
(62) Graber, T. A.; Morales, J. W.; Robles, P. A.; Galleguillos, H. R.; Taboada, M. E. Behavior of $LiOH{\cdot}H_2O$ crystals obtained by

https://doi.org/10.1021/acsomega.1c05379
ACS Omega 2021, 6, 33075−33084

evaporation and by drowning out. *Cryst. Res. Technol.* **2008**, *43*, 616−625.
(63) Gao, W.; Zhang, X.; Zheng, X.; Lin, X.; Cao, H.; Zhang, Y.; Sun, Z. Lithium carbonate recovery from cathode scrap of spent lithium-ion battery: A closed-loop process. *Environ. Sci. Technol.* **2017**, *51*, 1662−1669.
(64) Kondo, A.; Kurosawa, R.; Ryu, J.; Matsuoka, M.; Takeuchi, M. Investigation on the mechanisms of $Mg(OH)_2$ dehydration and MgO hydration by near-infrared spectroscopy. *J. Phys. Chem. C* **2021**, *125*, 10937−10947.
(65) Baïkov, Y. M. Self-diffusion of lithium, hydrogen, and oxygen ions in crystalline lithium hydroxide. *Phys. Solid State* **2010**, *52*, 2044−2057.
(66) Hermann, A.; Ashcroft, N. W.; Hoffmann, R. Lithium hydroxide, LiOH, at elevated densities. *J. Chem. Phys.* **2014**, *141*, 024505.
(67) Wenger, M.; Armbruster, T. Crystal chemistry of lithium: oxygen coordination and bonding. *Eur. J. Mineral.* **1991**, *3*, 387−400.
(68) Wang, X.; Andrews, L. Infrared spectra and electronic structure calculations for the group 2 metal $M(OH)_2$ dihydroxide molecules. *J. Phys. Chem. A* **2005**, *109*, 2782−2792.
(69) Hase, Y. Infrared active vibration modes of lithium hydroxide monohydrate. *Inorg. Nucl. Chem. Lett.* **1980**, *16*, 159−163.
(70) Hase, Y. Raman spectroscopic study of four isotopically substituted lithium hydroxide monohydrates. *Monatsh. Chem.* **1981**, *112*, 73−82.
(71) Gennick, I.; Harmon, K. M. Hydrogen bonding. VI. Structural and infrared spectral analysis of lithium hydroxide monohydrate and cesium and rubidium hydroxide hydrates. *Inorg. Chem.* **1975**, *14*, 2214−2219.
(72) Di Pietro, E.; Pagliai, M.; Cardini, G.; Schettino, V. Solid-state phase transition induced by pressure in $LiOH{\cdot}H_2O$. *J. Phys. Chem. B* **2006**, *110*, 13539−13546.
(73) Jones, L. H. The infrared spectra and structure of LiOH, $LiOH{\cdot}H_2O$ and the deuterium species. Remark on fundamental frequency of OH^-. *J. Chem. Phys.* **1954**, *22*, 217−219.
(74) Buchanan, R. A.; Kinsey, E. L.; Caspers, H. H. Infrared-Absorption Spectra of LiOH and LiOD. *J. Chem. Phys.* **1962**, *36*, 2665−2675.
(75) Yoshida, I. V. P.; Hase, Y. Infrared active frequencies for lithium hydroxide. *Spectrosc. Lett.* **1979**, *12*, 409−414.
(76) Parker, S. F.; Refson, K.; Bewley, R. I.; Dent, G. Assignment of the vibrational spectra of lithium hydroxide monohydrate, $LiOH{\cdot}H_2O$. *J. Chem. Phys.* **2011**, *134*, 084503.
(77) Veerman, A.; Lee, H. M.; Kim, K. S. Dissolution nature of the lithium hydroxide by water molecules. *J. Chem. Phys.* **2005**, *123*, 084321.
(78) Pratihar, S.; Chandra, A. Microscopic solvation of a lithium atom in water-ammonia mixed clusters: Solvent coordination and electron localization in presence of a counterion. *J. Chem. Phys.* **2008**, *129*, 024511.

https://doi.org/10.1021/acsomega.1c05379
ACS Omega 2021, 6, 33075−33084